Eleventh International Conference on Computational Fluid Dynamics (ICCFD11), Maui, Hawaii, USA, July 11-15, 2022

ICCFD11-2022-0701

A Multi-Physics Modeling Framework for Plasma Wind Tunnels

A. Munafò*, V. Le Maout*, S. Kumar*, R. Chiodi*,
F. Panerai*, K. Stephani*, D. J. Bodony*, and M. Panesi*
Corresponding author: munafo@illinois.edu

* Center for Hypersonics and Entry Systems Studies (CHESS)
University of Illinois at Urbana-Champaign, Urbana IL, USA.

Abstract: This work discusses the development of a multi-physics modeling framework for inductively coupled plasma (ICP) wind tunnels. As opposed to a monolithic approach, separate in-house solvers are considered to deal with the different parts of the complete model. The flowfield is modeled using HEGEL, a finite volume solver for non-equilibrium plasmas. The simulation of the electric field and the thermal protection system (TPS) material sample is accomplished via a finite element and a finite volume solvers (FLUX and PATO, respectively). The three tools are coupled using the preCICE library. Results for two-dimensional axi-symmetric configurations are presented and discussed to illustrate the effectiveness of the proposed coupled approach for modeling ICP discharges along with material response and electromagnetic phenomena.

Keywords: Multi-physics, Numerical Algorithms, Computational Fluid Dynamics.

1 Introduction

Inductively coupled plasmas (ICPs) have broad range of applications which include spray processes [1], waste treatment [2], arc welding [3], plasma cutting [4], nanopowder fabrication [5] and testing of thermal protection system (TPS) materials for atmospheric entry vehicles.

In the above situations plasmas are mostly generated by means of a suitably designed torch. In its simplest configuration, a plasma torch consists of a tube made of quartz surrounded by an inductor coil made of a series of parallel current-carrying rings. The radio-frequency currents running through the inductor induce toroidal currents in the gas which is heated thanks to Ohmic dissipation [6, 7]. If the energy supplied is large enough to cause breaking of chemical bonds, the gas flowing through the torch can undergo ionization, thereby forming a plasma with temperatures up to, or above, 10 000 K. Since the heating of the initially low temperature gas occurs via electromagnetic induction, ICPs are essentially contamination-free. This not the case, for instance, of arc-jet facilities where material fragments resulting from electrode erosion may severely pollute the plasma with undesirable effects on diagnostics techniques (*e.g.*, emission/absorption spectroscopy).

Inductively coupled plasmas at, or near, atmosphere pressures are often referred to as *thermal plasmas* [8] since, due to the large pressures, the high collision rates among free-electrons and

heavy-particles (*e.g.*, atoms and molecules) ensure that their temperatures are nearly equal. On this basis, large pressure ICPs are often modeled assuming local thermodynamic equilibrium (LTE). This choice is attractive from both the modeling and computational point of view as the fluid governing equations remain the global mass, momentum and energy balance relations [9–14].[1] The only complication stems from pressure and temperature dependence of thermodynamic and transport properties. However, this may be tackled by means of tabulation or fitting during pre-processing [15].

Despite its popularity, there exist situations where the LTE assumption for ICPs breaks down. Aside from low pressure discharges, non-local thermodynamic equilibrium (NLTE) effects may be important even around atmospheric pressure. This is the case, for instance, of the fringe region of a plasma jet where the cold chamber gas is entrained by the hot (and usually laminar) plasma core exiting the torch [16]. The ensuing mixing, which eventually leads to a fully turbulent flow, is inherently a NLTE process involving diffusion along with recombination and de-excitation reactions. Also, despite thermal non-equilibrium effects may be negligible at the torch exit, the plasma state may still be affected by NLTE in the discharge [17–19]. Under these circumstances, LTE simulations tend to overestimate temperatures, with consequent large errors on chemical composition. These facts must be taken into account when comparing predicted temperatures with experiments.

As it may be inferred from the previous discussion, the self-consistent modeling of an ICP wind tunnel is inherently a multi-physics problem which requires coupling between electromagnetic fields, NLTE hydrodynamics and material response. Moreover, it must be borne in mind that an actual ICP facility is always characterized by a certain degree of unsteadiness as a result of turbulence and/or arc restrikes [20]. Despite this simulations are mostly performed under steady-state using engineering turbulence models (*e.g.*, RANS).

The purpose of this paper is the development of a computational multi-physics framework for ICP wind tunnels. Instead of adopting a monolithic approach the hydrodynamics, electromagnetic field and material response are handled by separate solvers developed either within the Center for Hypersonics and Entry Systems Studies (CHESS) at University of Illinois, or by external collaborators. Hydrodynamics is modeled using HEGEL [21], a finite volume solver for LTE/NLTE plasmas. The simulation of the electric field and the TPS material sample is accomplished via a finite element and a finite volume solvers (FLUX [22] and PATO [23], respectively). Coupling is realized by means of the preCICE [24] open-source library.

The paper is structured as follows. Section 2 describes the physical model. The coupled computational framework is discussed in Sec. 3. Verification tests and applications are presented in Sec. 4. Conclusions and future work are outlined in Sec. 5.

2 Physical Model

The plasmas considered in this work are made of electrons, neutrals and ions, and are modeled as mixtures of ideal gases in NLTE conditions (see Sec. 2.1). The LTE formulation, used for the purpose of comparison, maybe deduced from the NLTE description and is discussed in detail in monographs available in the literature (*e.g.*, Ref. [8]). Section 2.2 treats the modeling of the electromagnetic field. The mathematical modeling of the TPS material sample may be found elsewhere [23].

[1] This is true as long demixing is neglected.

2.1 Plasma

As already recalled in Sec. 1, the modeling of a dilute LTE plasma is mathematically equivalent to that of a pure gas with temperature and pressure dependent properties. This approach, very appealing from the computational perspective, may lead, however, to a poor description when non-equilibrium effects prevail. Under this situation one has to keep track of how the main chemical constituents of a plasma evolve as a result of convection, diffusion and kinetic processes and, eventually, account for non-Boltzmann distributions of their internal degrees of freedom (*e.g.*, electronic states) [25, 26].

Before going through the details, it is helpful to introduce some notation. The species the plasma is made of are stored in set $\mathcal{S} = \{\mathrm{e}\} \cup \mathcal{S}_\mathrm{h}$, where the symbol e denotes free-electrons. The heavy-particle subset $\mathcal{S}_\mathrm{h}$ contains atoms and molecules: $\mathcal{S}_\mathrm{h} = \mathcal{S}_\mathrm{a} \cup \mathcal{S}_\mathrm{m}$. Here the word species may refer to chemical components such as N_2 or NO^+ when considering a conventional multi-temperature (MT) formulation [25], or individual bound-states/groups (*e.g.*, $\mathrm{N}(i)$) for a collisional-radiative (CR) [26–41] or grouping approach [42–56]. In both circumstances, heavy-particles and free-electrons are assigned distinct translational temperatures (T_h and T_e, respectively) to account for the inefficient energy transfer, due to the large mass disparity, in electron-heavy collisions.

The NLTE governing equations, along with constitutive relations for thermodynamics, transport and kinetics, are obtained via the Chapman-Enskog (CE) expansion method for the Boltzmann equation of Kinetic Theory [57–65]). Here the expansion is stopped at first-order which allows to retrieve Newton and Fourier's law for molecular transport of momentum and energy, respectively, in the case of a pure gas composed of structureless particles. Kinetic processes (*e.g.*, ionization) are treated under the assumption of a Maxwellian reaction regime [58, 59, 65].

Thermodynamics In view of the ideal gas assumption (*e.g.*, no pressure ionization [66]), the pressure of the plasma follows from Dalton's law:

$$p = p_\mathrm{h} + p_\mathrm{e}, \tag{1}$$

where the free-electron and heavy-particle partial pressures are, respectively, $p_\mathrm{h} = n_\mathrm{h} k_\mathrm{B} T_\mathrm{h}$ and $p_\mathrm{e} = n_\mathrm{e} k_\mathrm{B} T_\mathrm{e}$, with k_B being Boltzmann's constant. The symbols n_e and n_h stand, respectively, for the number density of free-electrons and heavy-particles. The latter quantity is obtained from $n_\mathrm{h} = \sum_{s \in \mathcal{S}_\mathrm{h}} n_s$. Upon introducing the mole fractions $X_s = n_s/n$, the number density of the plasma as a whole may be retrieved from Eq. (1):

$$n = \frac{p}{k_\mathrm{B} T_\mathrm{h} \left[1 + X_\mathrm{e} \left(T_\mathrm{e}/T_\mathrm{h} - 1\right)\right]}. \tag{2}$$

The plasma density is $\rho = \sum_{s \in \mathcal{S}} \rho_s$, where the partial densities are related to the number densities via $\rho_s = m_s n_s$, with m_s being the (particle) mass of s.

The energy per unit-mass of the individual species may be written as [67, 68]:

$$e_s = \begin{cases} e_s^\mathrm{tr}(T_\mathrm{e}), & s = \mathrm{e}, \\ \\ e_s^\mathrm{tr}(T_\mathrm{h}) + e_s^\star + \Delta h_s^\mathrm{f}, & s \in \mathcal{S}_\mathrm{h}, \end{cases} \tag{3}$$

where translational contribution is computed classically based on the principle of equipartition of energy: $e_s^\mathrm{tr}(T) = 3/2(k_\mathrm{B} T/m_s)$ [69]. The symbol Δh_s^f denotes the absolute formation enthalpy and accounts for both formation and excitation (when using a CR approach). The remaining term, $e_s^\star$, accounts for the energy of the *thermalized* internal degrees of freedom (*e.g.*, rotation,

vibration) stored in the set $\mathcal{G}$:

$$e_s^\star = e_s^\star(\tilde{T}_1, \ldots, \tilde{T}_m) = \sum_{g \in \mathcal{G}} e_{sg}^\star(\tilde{T}_1, \ldots, \tilde{T}_m), \quad s \in \mathcal{S}_\mathrm{h}, \tag{4}$$

where $\tilde{T}_1, \ldots, \tilde{T}_m$ are the internal temperatures (*e.g.*, vibrational, electronic) of the NLTE formulation being considered (*e.g.*, multi-temperature, grouping). To help elucidating the discussion some specific forms of $e_s^\star$ are here given. For a conventional two-temperature formulation [70], the expression of $e_s^\star$ for a diatomic molecule described by the rigid-rotor and harmonic oscillator models is [71, 72]:

$$e_s^\star(T_\mathrm{r}, T_\mathrm{v}) = \frac{k_\mathrm{B}}{m_s} T_\mathrm{r} + \frac{k_\mathrm{B}}{m_s} \frac{\theta_s^\mathrm{v}}{\left[\exp\left(\theta_s^\mathrm{v}/T_\mathrm{v}\right) - 1\right]}, \quad s \in \mathcal{S}_\mathrm{m}, \tag{5}$$

where T_r and T_v are, respectively, the rotational and vibrational temperatures, whereas θ_s^v is the characteristic vibrational temperature. On the other hand, for a *rovibronic* CR model, where all bound states are treated as separate species, $e_s^\star$ is zero.

Collecting the above formulae, the energy per unit-mass of the plasma, free-electrons, and the *thermalized* internal degrees of freedom may be written as:

$$e = \sum_{s \in \mathcal{S}_\mathrm{h}} y_s \left[e_s^\mathrm{tr}(T_\mathrm{h}) + \Delta h_s^\mathrm{f} \right] + \sum_{g \in \mathcal{G}} \tilde{e}_g + \tilde{e}_\mathrm{e}, \tag{6a}$$

$$\tilde{e}_g = \sum_{s \in \mathcal{S}_\mathrm{h}} y_s e_{sg}^\star(\tilde{T}_1, \ldots, \tilde{T}_m), \quad g \in \mathcal{G}, \tag{6b}$$

$$\tilde{e}_\mathrm{e} = y_\mathrm{e} e_\mathrm{e}^\mathrm{tr}(T_\mathrm{e}), \tag{6c}$$

where the mass fractions are $y_s = \rho_s/\rho$.

Transport The application of the CE solution method yields explicit expressions for transport fluxes. In the first-order approximation, these fluxes are linearly related to gradients of macroscopic quantities such as velocity and temperatures, the proportionality factors being the so called transport properties or coefficients. The formulae for the latter are given by *bracket* integrals which are practically evaluated using a Sonine-Laguerre polynomial expansion [57, 58]. Here only the main results are quoted. The interested reader may consult the above references on Kinetic Theory for the details. In what follows secondary effects such as thermal diffusion are neglected. These are however available in the developed ICP framework.

As anticipated above, viscous stresses are given by Newton's law:

$$\tau_{ij} = \mu \left(\frac{\partial u_i}{\partial x_j} + \frac{\partial u_j}{\partial x_i} - \frac{2}{3} \delta_{ij} \frac{\partial u_k}{\partial x_k} \right), \tag{7}$$

where u_i denotes the velocity component along the i-th direction, whereas δ_{ij} stands for Kronecker's delta. In the first Sonine-Laguerre approximation, the dynamic viscosity reads [58]:

$$\mu = \sum_{s \in \mathcal{S}_\mathrm{h}} z_s^\mu X_s. \tag{8}$$

The z_s^μ are solution of the symmetric system:

$$\sum_{p \in \mathcal{S}_\mathrm{h}} G_{sp}^\mu z_p^\mu = X_s, \quad s \in \mathcal{S}_\mathrm{h}, \tag{9}$$

where $G^{\mu}_{sp} = G^{\mu}_{ps}$ are the entries of the viscosity transport matrix. Free-electrons do not contribute to viscous stresses due to their small mass [60].

The diffusion velocities V^i_s satisfy Stefan-Maxwell's equations:

$$\sum_{p\in\mathcal{S}} G^V_{pe} V^i_p - \kappa_e \frac{T_h}{T_e} E_i = -d^i_e \frac{T_h}{T_e}, \tag{10a}$$

$$\sum_{p\in\mathcal{S}} G^V_{ps} V^i_p - \kappa_s E_i = -d^i_s, \quad s \in \mathcal{S}_h, \tag{10b}$$

where $G^V_{sp} = G^V_{ps}$ are the entries of the symmetric Stefan-Maxwell matrix, whereas E_i is the i-th component of the electric field. The latter accounts, in general, for both external sources and charge distribution within the plasma (*i.e.*, self-induced electric field). The κ_s are defined as $\kappa_s = (X_s Q_s - y_s Q)/k_B T_h$, where the plasma charge is $Q = \sum_{s\in\mathcal{S}} X_s Q_s$, where Q_s denotes the charge of species s. The modified diffusion driving forces in Eqs. (10) are:

$$d^i_s = \frac{p}{n k_B T_h}\left(\frac{\partial X_s}{\partial x_i}\right) + \frac{X_s - y_s}{n k_B T_h}\left(\frac{\partial p}{\partial x_i}\right), \quad s \in \mathcal{S}. \tag{11}$$

It is worth mentioning that the d^i_s are not independent since $\sum_{s\in\mathcal{S}} d^i_s = 0$, as shown by a direct calculation. For ICP simulations, Eq. (11) may be simplified as follows. Since the pressure in both chamber and torch is essentially constant, the second term on the right-hand-side may be dropped. Further, if the differences between heavy-particle and free-electron temperatures are not too large, the pressure becomes $p \simeq n k_B T_h$, which leads to $d^i_s \simeq \partial X_s/\partial x_i$.

The diffusion velocities are found by solving Eqs. (10) along with mass conservation and ambipolar diffusion constraints, which may be combined together as $\sum_{s\in\mathcal{S}} \kappa_s V^i_s = 0$ [62]. The solution of Eqs. (10) along with the previous relation yields both diffusion velocities and (ambipolar) electric field.

For a multi-component NLTE plasma, the total, internal, and free-electron heat-flux components account for both heat conduction and mass diffusion, and read:

$$q_i = -\lambda_h \left(\frac{\partial T_h}{\partial x_i}\right) + \sum_{s\in\mathcal{S}_h} J^i_s \left[h^{tr}_s(T_h) + \Delta h^f_s\right] + \sum_{g\in\mathcal{G}} \tilde{q}^g_i + q^e_i, \tag{12a}$$

$$\tilde{q}^g_i = -\tilde{\lambda}_g \left(\frac{\partial \tilde{T}_g}{\partial x_i}\right) + \sum_{s\in\mathcal{S}_h} J^i_s \, e^{\star}_{sg}(\tilde{T}_1, \ldots, \tilde{T}_m), \quad g \in \mathcal{G} \tag{12b}$$

$$q^e_i = -\lambda_e \left(\frac{\partial T_e}{\partial x_i}\right) + J^i_e h^{tr}_e(T_e), \tag{12c}$$

where the translation enthalpies and the mass diffusion fluxes are $h^{tr}_s(T) = e^{tr}_s(T) + k_B T/m_s$ and $J^i_s = \rho_s V^i_s$, respectively.

The translational conductivity of heavy-particles is evaluated in the second Sonine-Laguerre approximation:

$$\lambda_h = \sum_{s\in\mathcal{S}_h} z^{\lambda}_s X_s, \tag{13}$$

where, as for the viscosity, the z^{λ}_s are solution of a linear symmetric system:

$$\sum_{p\in\mathcal{S}_h} G^{\lambda}_{sp} z^{\lambda}_p = X_s, \quad s \in \mathcal{S}_h, \tag{14}$$

with $G^{\lambda}_{sp} = G^{\lambda}_{ps}$ being the entries of the heavy thermal conductivity transport matrix [58]. For free-electrons, a third-order Sonine approximation is instead considered [60, 62]:

$$\lambda_{\mathrm{e}} = \frac{75}{64} k_{\mathrm{B}} X_{\mathrm{e}}^2 \sqrt{\frac{2\pi k_{\mathrm{B}} T_{\mathrm{e}}}{m_{\mathrm{e}}}} \frac{\Lambda^{22}_{\mathrm{ee}}}{\Lambda^{11}_{\mathrm{ee}}\Lambda^{22}_{\mathrm{ee}} - \Lambda^{12}_{\mathrm{ee}}\Lambda^{21}_{\mathrm{ee}}}, \tag{15}$$

where $\Lambda^{ij}_{\mathrm{ee}} = \Lambda^{ji}_{\mathrm{ee}}$ are the entries of the electron subsystem transport matrix [21, 62]. The contribution to thermal conductivity of the internal *thermalized* degrees of freedom, $\tilde{\lambda}_g$, is modeled by means of the generalized Eucken correction [58, 65].

The conduction current within the plasma is modeled based on Ohm's law:

$$j_i = \sigma_{\mathrm{e}}\, E_i, \tag{16}$$

where the electrical conductivity is (second Sonine-Laguerre approximation) [62]:

$$\sigma_{\mathrm{e}} = \frac{3}{8} \frac{X_{\mathrm{e}}^2 Q_{\mathrm{e}}^2}{k_{\mathrm{B}} T_{\mathrm{e}}} \sqrt{\frac{2\pi k_{\mathrm{B}} T_{\mathrm{e}}}{m_{\mathrm{e}}}} \frac{\Lambda^{11}_{\mathrm{ee}}}{\Lambda^{00}_{\mathrm{ee}}\Lambda^{11}_{\mathrm{ee}} - \Lambda^{01}_{\mathrm{ee}}\Lambda^{10}_{\mathrm{ee}}}. \tag{17}$$

Kinetics The NLTE kinetics scheme includes the *rate* processes below:

- dissociation by heavy-particle and electron impact,
- particle and charge exchange (*e.g.*, Zel'dovich reactions),
- ionization and excitation by electron impact,
- associative ionization and dissociative recombination,
- elastic energy transfer in electron-heavy collisions.

Radiative processes such as line emission and absorption are not taken into account.

The mass and energy source terms due to kinetic processes follow, again, from the CE method. Since a Maxwellian reaction regime is assumed, the source terms are obtained via moments of the collision operator in the Boltzmann equation with the distribution function taken as Maxwell-Boltzmann at the appropriate temperature [58, 59].

Governing equations Upon collecting the content of the above paragraphs, it is possible to write down the governing equations for the NLTE plasmas treated in this work [17, 18, 73]:

$$\frac{\partial \mathbf{U}}{\partial t} + \frac{\partial \mathbf{F}_j}{\partial x_j} - \frac{\partial \mathbf{D}_j}{\partial x_j} = \mathbf{S}. \tag{18}$$

The vectors storing conservative variables, inviscid and diffusive fluxes, and source terms read:

$$\mathbf{U} = \left[\begin{array}{ccccc} \rho_s & \rho u_i & \rho E & \rho \tilde{e}_g & \rho \tilde{e}_{\mathrm{e}} \end{array} \right]^{\mathrm{T}}, \tag{19a}$$

$$\mathbf{F}_i = \left[\begin{array}{ccccc} \rho_s u_i & p\delta_{ij} + \rho u_i u_j & \rho u_i H & \rho u_i \tilde{e}_g & \rho u_i \tilde{e}_{\mathrm{e}} \end{array} \right]^{\mathrm{T}}, \tag{19b}$$

$$\mathbf{D}_i = \left[\begin{array}{ccccc} -J^i_s & \tau_{ji} + f^{\mathrm{L}}_i & \tau_{ij} u_j - q_i & -\tilde{q}^g_i & -q^{\mathrm{e}}_i \end{array} \right]^{\mathrm{T}}, \tag{19c}$$

$$\mathbf{S} = \left[\begin{array}{ccccc} \omega_s & 0 & \Omega^{\mathrm{J}} & \tilde{\Omega}_g & \tilde{\Omega}_{\mathrm{e}} + \Omega^{\mathrm{J}} - p_{\mathrm{e}} \partial u_k / \partial x_k \end{array} \right]^{\mathrm{T}}, \quad s \in \mathcal{S}, \quad g \in \mathcal{G}, \tag{19d}$$

where the total energy and enthalpy per unit-mass are $E = e + u_i u_i/2$ and $H = E + p/\rho$, respectively. The Lorentz force, f^{L}_i, and the Joule heating, Ω^{J}, account for the interaction between the plasma and the electromagnetic field (see Sec. 2.2), whereas the mass production

terms, ω_s, and the energy transfer terms, $\tilde{\Omega}_g$ and $\tilde{\Omega}_\mathrm{e}$, represent the effects of kinetic processes on the mass and energy balance of the plasma.

2.2 Electromagnetic field

The electromagnetic field inside an ICP facility is governed by Maxwell's equations. To make the problem tractable, the following assumptions are hereby introduced [11, 74, 75]:

- Low frequency approximation. The inductor frequency is much smaller than that of the plasma (*i.e.*, $f \ll f_p$), allowing to rule out both electrostatic and electromagnetic waves.
- The plasma is quasi-neutral, unmagnetized and collision dominated.
- Low magnetic Reynolds number (*i.e.*, negligible Hall currents).

Frequency domain formulation In this work Maxwell's equations are solved assuming a harmonic time-dependence of all electromagnetic quantities:

$$\mathbf{E}(\mathbf{r}, t) = \mathbf{E}_\mathrm{c}(\mathbf{r}) \exp(\imath\, \omega t), \tag{20}$$

where $\imath$ denotes the imaginary unit. In the above relation the subscript c denotes a phasor (*i.e.*, complex quantity) and $\omega = 2\pi f$ [11]. The use of Eq. (20) and a similar relation for the magnetic induction in Maxwell's equations along with the above assumptions, leads to the following equation for the complex amplitude of the electric field:

$$\nabla \times \nabla \times \mathbf{E}_\mathrm{c} + \imath \mu_0 \sigma \omega \mathbf{E}_\mathrm{c} = -\imath \mu_0 \omega \mathbf{J}_s, \tag{21}$$

where μ_0 is the permeability of free space. The electrical conductivity, σ, is the one of the plasma (Eq. (17)) inside the torch, whereas it is assumed zero anywhere else. The vector $\mathbf{J}_s$ on the right-hand-side of the Eq. (21) is the current density of external sources (*e.g.*, inductor coils). Here $\mathbf{J}_s$ is modeled by means of a N-point source model [74, 75]:

$$\mathbf{J}_s = \mathbf{J}_0 \sum_{i=1}^{N} \delta(\mathbf{r} - \mathbf{r}_i), \tag{22}$$

where N is the number of coils, $\mathbf{r}_i$ the location of the center of the i-th coil, whereas δ denotes Dirac's delta function. Following the work by Boulos [9], the current density in each coil, $\mathbf{J}_0$, is updated to match a target value of the power dissipated by Joule heating:

$$P_t = \int \Omega^\mathrm{J} dv. \tag{23}$$

Once the electric field amplitude known, the magnetic induction may be retrieved via Faraday's law allowing, in turn, to compute the Lorentz force and Joule heating in the fluid governing equations (see Eq. (19d)). Since an ICP is designed to operate at frequencies of the order of MHz, it is reasonable to assume that, on a *macroscopic scale*, the plasma effectively experiences a time-averaged Lorentz force and Joule heating [11, 74, 75]:

$$\left\langle \mathbf{f}^\mathrm{L} \right\rangle = \frac{1}{2} \left(\frac{\sigma}{\omega} \right) \left[\mathbf{E}_\mathrm{c} \times (i \nabla \times \mathbf{E}_\mathrm{c})^* \right], \tag{24a}$$

$$\left\langle \Omega^\mathrm{J} \right\rangle = \frac{1}{2} \sigma \mathbf{E}_\mathrm{c} \cdot \mathbf{E}_\mathrm{c}^*, \tag{24b}$$

where the $*$ superscript denotes the complex conjugate.

3 Computational framework

The multi-physics model for ICP wind tunnels is built by coupling three solvers responsible for: (i) the plasma, (ii) the electromagnetic field, and (iii) the thermophysical properties of the TPS sample. Compared to a monolithic approach, this strategy has certain advantages such as reducing software complexity and maintenance work, and choosing the most suitable method for each sub-problem. The main features of the three solvers are outlined below.

3.1 Solvers

Plasma The plasma solver is HEGEL (High-fidElity tool for maGnEto-gasdynamics simuLations), a parallel multi-block structured code for LTE/NLTE plasmas written in modern object oriented `Fortran` 2008 [21, 76]. Distribution of data among processes is performed using MPI along with the functionalities and data structures provided by the PETSC library [77–79]. The evaluation of thermodynamic and transport properties, and source terms is accomplished via the PLATO (PLAsmas in Thermodynamic nOn-equilibrium) library [21].

The flow governing equations (19) are discretized in space based on the finite volume method [80]:

$$V_{ijk}\frac{d\hat{\mathbf{U}}_{ijk}}{dt}+\sum_{f\in\mathcal{F}_{ijk}}\left(\tilde{\mathbf{H}}^{\mathrm{i}}_{f}-\tilde{\mathbf{H}}^{\mathrm{d}}_{f}\right)A_f=V_{ijk}\,\mathbf{S}_{ijk}, \tag{25}$$

where $\hat{\mathbf{U}}_{ijk}$ denotes the volume-averaged conservative variables of cell (i,j,k), with V_{ijk} and A_f being, respectively, the corresponding volume and face areas (stored in the set $\mathcal{F}_{ijk}$). The symbols $\tilde{\mathbf{H}}^{\mathrm{i}}_{f}$ and $\tilde{\mathbf{H}}^{\mathrm{d}}_{f}$ stand, respectively, for the inviscid and diffusive fluxes at face f.

Inviscid fluxes are evaluated using flux functions such as Roe's approximate Riemann solver [81] or the AUSM-family method [82] along with reconstruction procedures such as MUSCL [83, 84] or WENO [85] to achieve high-order accuracy. Diffusive fluxes are evaluated using Green-Gauss' theorem to determine face-averaged gradients. The semi-discrete system (25) is integrated in time via explicit, implicit or implicit-explicit (IMEX) methods [21].

Electromagnetic field The equation governing the spatial dependence of the electric field amplitude (21) is solved using FLUX [22], a `C++` MFEM-based [86, 87] mixed finite element solver for time- and frequency-domain electromagnetics.

The discretization of Eq. (21) starts from its weak form assuming a conforming unstructured finite element mesh composed of either tetrahedrons, hexahedrons or prisms [88]. For a general three-dimensional field, the electric field amplitude is a 1-form and thus approximated as:

$$\mathbf{E}_c(\mathbf{r})=\sum_{i=1}^{n}e_i\,\mathbf{W}^1_i(\mathbf{r}), \tag{26}$$

where e_i is the i-th degree of freedom, whereas $\mathbf{W}^1_i$ are 1-form basis functions. To obtain the weak form, Eq. (21) is multiplied by a test function $\mathbf{W}^1_j$, and integrated over the domain:

$$\langle\nabla\times\mathbf{W}^1_i,\nabla\times\mathbf{W}^1_j\rangle+\imath\omega\mu_0\langle\sigma\mathbf{W}^1_i,\mathbf{W}^1_j\rangle=-\imath\omega\mu_0\langle\mathbf{J}_s,\mathbf{W}^1_j\rangle. \tag{27}$$

The large sparse linear system resulting from Eq. (27) is solved in MFEM using the HYPRE library [89].

Material sample The evolution of the thermophysical properties of the TPS sample is modeled using PATO [23], a `C++` OpenFOAM-based [90] finite volume solver for porous media.

3.2 Multi-physics coupling

The coupling between HEGEL, FLUX and PATO is realized in practice using the preCICE open source library [24]. Figure 1 shows the data being exchanged between the solvers. For an ICP simulation two types of coupling are to be considered.

- Surface coupling (material sample). Here HEGEL sends PATO the normal projection of the heat, momentum and mass diffusion fluxes, and receives the global blowing rate, mass fractions and temperature. These quantities are used then to retrieve surface pressure, density and velocity as in Refs. [91, 92].
- Volume coupling (torch). In this case FLUX receives from HEGEL the plasma electrical conductivity, which is used to compute the electric field. Once this step completed, the Lorentz force and Joule heating are evaluated and sent to HEGEL.

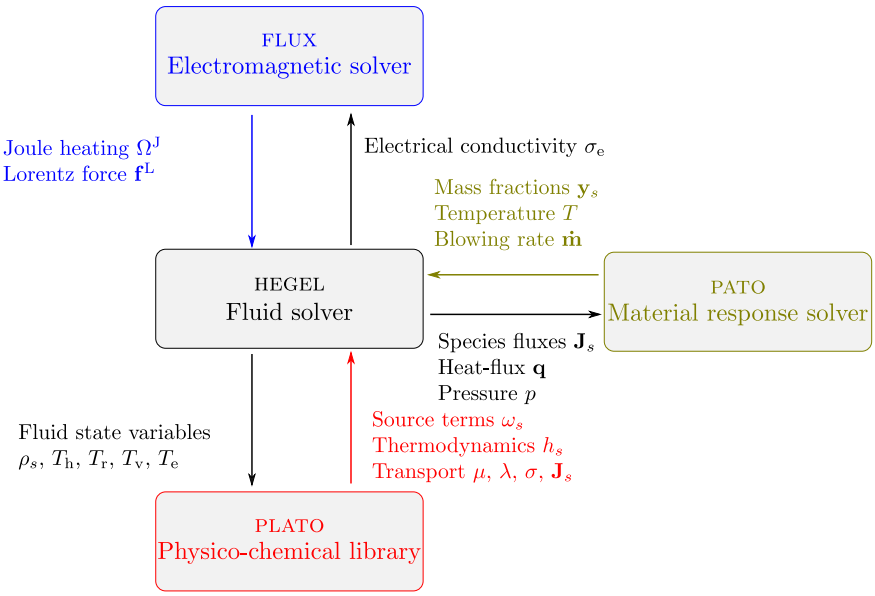

Figure 1: Solver coupling schematic.

4 Applications

This Section discusses applications of the ICP framework described in Sec. 3. Verification benchmarks are first presented in Sec. 4.1. This is followed by applications to axi-symmetric ICP configurations in Secs. 4.2 and 4.3.

4.1 Verification benchmarks

Conjugate heat transfer The first benchmark consists in solving the heat equation for a homogeneous and isotropic medium on a square domain (see Figure 2), to test and verify the communication of surface data. The box is partitioned in two and filled with air treated as a calorically perfect gas. The thermal conductivity is constant and set to $0.0262\,\mathrm{W/m\,K}$, whereas the box side length (L) is $0.02\,\mathrm{m}$.

The heat equation is solved using a stepwise initial temperature profile:

$$T(x, y, 0) = \begin{cases} T_l, & x \in [0, L/2) \text{ and } y \in [0, L], \\ T_r, & x \in (L/2, L] \text{ and } y \in [0, L], \end{cases} \tag{28}$$

with T_l and T_r set, respectively, to 300 K and 500 K. The left ($x = 0$) and right ($x = L$) walls are isothermal with temperatures kept at T_l and T_r, respectively, whereas the upper and lower walls are adiabatic. In light of the chosen initial and boundary conditions the problem is one-dimensional and has a simple analytical solution (see App. A).

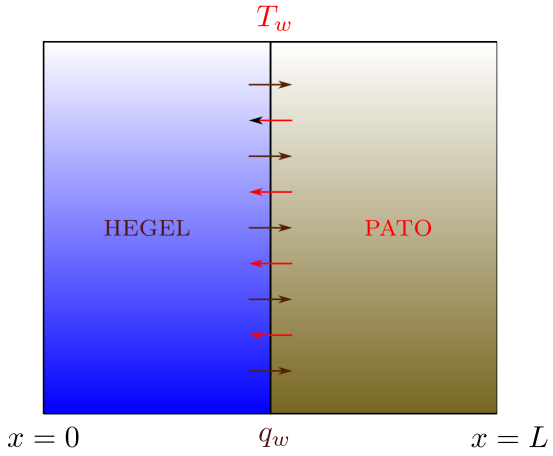

Figure 2: Conjugate heat transfer coupling benchmark: simulation settings.

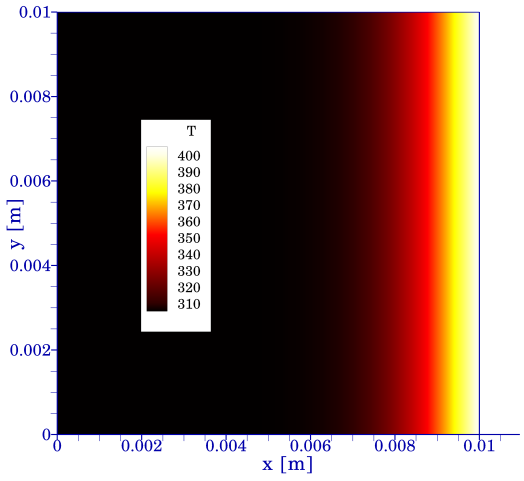

(a) Temperature at $t = 50$ ms (fluid domain).

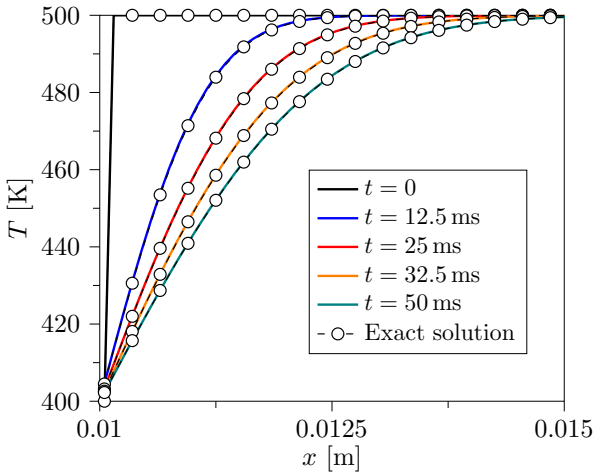

(b) Temperature history (solid domain).

Figure 3: Conjugate heat transfer coupling benchmark: in (a) temperature at $t = 50$ ms (fluid domain), in (b) time history of temperature in the solid domain.

In the current simulation HEGEL sends/receives heat flux/temperature to/from PATO. In both codes, the heat equation is evolved in time using Crank-Nicolson method [80]. The time-step is set to $\Delta t = 0.5$ ms, and data are exchanged using implicit coupling. The results in Figure 3 show an excellent agreement between the computed temperature distribution and the exact solution, confirming the correct implementation of surface coupling.

ICP torch with annular injection After assessing the correct exchange of surface data, volume coupling is verified by simulating the two-dimensional axi-symmetric LTE flow without swirl in a plasma torch with annular injection (see Figure 4). The working fluid is air. Both geometry and reference solution are taken from Ref. [74].

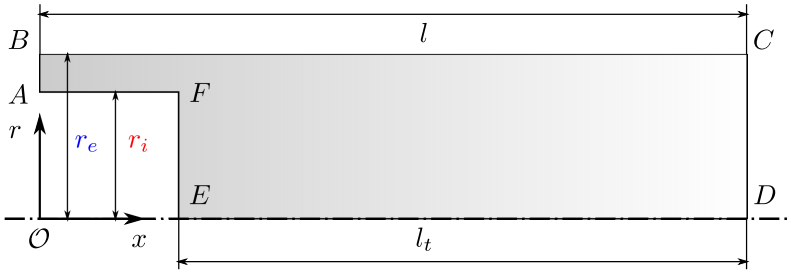

Figure 4: Schematic of the ICP torch with annular injection.

The boundary conditions for the plasma are as follows:

- inlet (AB):

$$\rho u = \frac{\dot{m}}{\pi \left(r_e^2 - r_i^2\right)}, \quad \frac{\partial p}{\partial x} = 0, \quad T = T_{in}, \tag{29}$$

- centerline (DE):

$$\frac{\partial \rho}{\partial r} = \frac{\partial u}{\partial r} = \frac{\partial p}{\partial r} = 0, \quad v = 0, \tag{30}$$

- walls (AF, EF and BC):

$$u = v = 0, \quad T = T_w \tag{31}$$

- exit (CD)

$$p = p_\infty. \tag{32}$$

The mass flow ($\dot{m}$) and exit pressure (p_∞) are 6 g/s and 5000 Pa, respectively, whereas the wall and inlet temperatures (T_w and T_{in}, respectively) are both set to 350 K. The target dissipated power (P_t) and the frequency (f) of the current running through the inductor are 50 kW and 0.45 MHz, respectively.

Figure 6 shows HEGEL and FLUX grids. In the torch, where communication among the two codes occurs, the nodes of both grids coincide. This is done for the purpose of higher accuracy. However, this is not a mandatory requirement. As a matter of fact, non-matching grids can be handled in preCICE [24] by means of radial basis functions or nearest-neighbour interpolation. The electric field is assumed zero on both the centerline and the farfield region.

Since the modeling of the plasma formation transient is out of the scope of this work, the calculation is started by imposing a high-temperature (*e.g.*, $T_{\max} \simeq 10\,000$ K) LTE plasma blob in the torch. After that, the fluid governing equations are marched in time using the backward Euler method [80] along with local time-stepping to accelerate convergence to steady-state [93]. Exchange of data between HEGEL and FLUX is performed at the end of each fluid time-step via explicit coupling. In the present case, data could be also exchanged every ten fluid time-steps without affecting convergence and/or stability of the solution.

Figure 6a shows the computed axial velocity and temperature distributions. The streamlines added on the top of the axial velocity field show the characteristic recirculation eddy resulting from electromagnetic pumping [11, 12]. The temperature is maximum on the axis, with peak values around 10 000 K, as also shown in Figure 6 which compares the present results with

literature [74]. Overall the agreement is very good with minor differences probably due to the use of a different database for thermodynamics (*e.g.*, electronic levels) and transport collision integrals. The radial temperature distribution is flat close to the axis as a result of neglecting radiation losses [19], and undergoes a series inflexion points. These are consequent of local maxima of the total thermal conductivity of air.

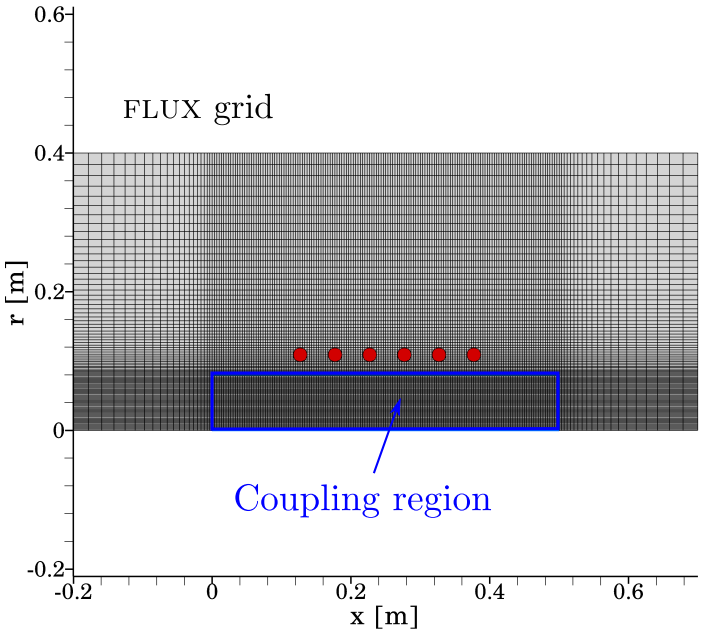

Figure 5: HEGEL and FLUX grids for ICP torch simulation. The area enclosed by the blue line is the volume coupling region, whereas the red circles highlight the coil locations.

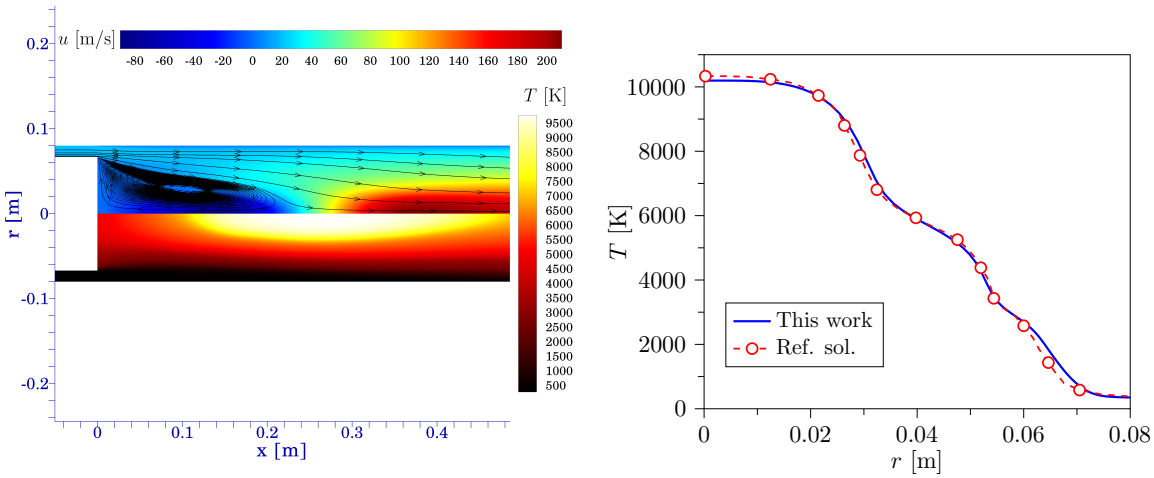

(a) Temperature and axial velocity fields.

(b) Radial temperature profile ($x = 0.265\,\mathrm{m}$).

Figure 6: ICP torch with annular injection: in (a) temperature and axial velocity fields with streamlines, in (b) comparison of radial temperature distribution ($x = 0.265\,\mathrm{m}$) with literature [74, 75] (LTE air plasma; $\dot{m} = 6\,\mathrm{g/s}$, $f = 0.45\,\mathrm{MHz}$, $P_t = 50\,\mathrm{kW}$, $p_\infty = 5000\,\mathrm{Pa}$, $T_w = 350\,\mathrm{K}$).

4.2 NLTE effects in a plasma torch

After verifying the implementation of surface and volume coupling, further applications are considered. The first consists in repeating the LTE torch simulation of Sec. 4.1 to assess the impact of non-equilibrium on quantities of interest (*e.g.*, temperature).

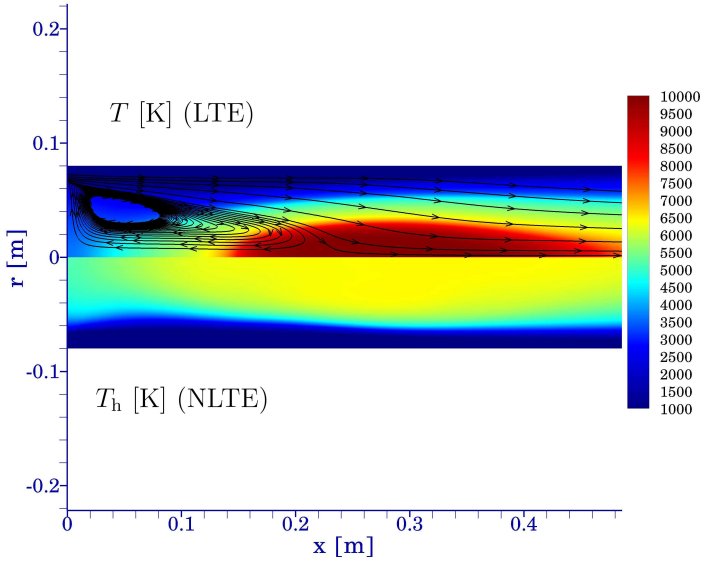

Figure 7: ICP torch with annular injection: comparison between LTE temperature (top) and NLTE heavy-particle temperature (bottom) distributions (LTE and NLTE air plasma; $\dot{m} = 6\,\mathrm{g/s}$, $f = 0.45\,\mathrm{MHz}$, $P_t = 50\,\mathrm{kW}$, $p_\infty = 5000\,\mathrm{Pa}$, $T_w = 350\,\mathrm{K}$).

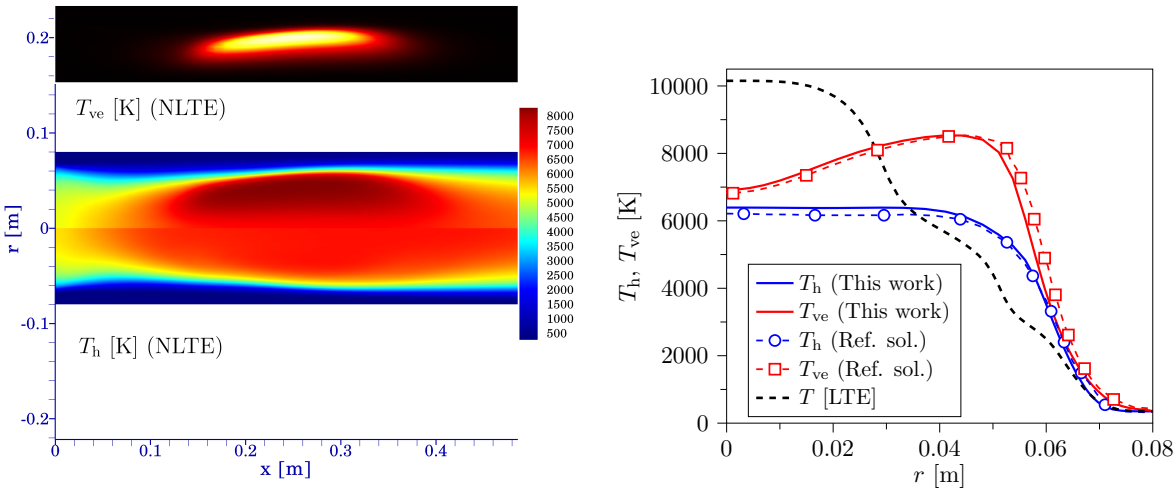

(a) Temperatures and Joule heating.

(b) Radial temperature profile ($x = 0.235\,\mathrm{m}$).

Figure 8: ICP torch with annular injection: in (a) vibronic and heavy-particle temperature, and joule heating, in (b) comparison of radial temperature distribution ($x = 0.235\,\mathrm{m}$) with literature [74] (NLTE air plasma; $\dot{m} = 6\,\mathrm{g/s}$, $f = 0.45\,\mathrm{MHz}$, $P_t = 50\,\mathrm{kW}$, $p_\infty = 5000\,\mathrm{Pa}$, $T_w = 350\,\mathrm{K}$).

The air plasma is made of N_2 and O_2, and their main dissociation and ionization products: $\mathcal{S} = \{e^-, N_2, O_2, NO, N, O, {N_2}^+, {O_2}^+, {NO}^+, {N}^+, {O}^+\}$. Non-equilibrium effects are taken into account based on the Park two-temperature model [70] along with Dunn and Kang reaction kinetics scheme [73]. The rate controlling temperature of chemical reactions (*e.g.*, dissociation, exchange) are taken from Ref. [74] to verify the implementation of the NLTE-related classes of HEGEL. It is important to mention that the NLTE model is built upon usage of the same database (*e.g.*, thermodynamics, transport) used for the LTE simulations. This ensures the self-consistency of the LTE vs NLTE comparison.

Figure 7 shows the temperature distribution in the torch. Compared to the NLTE simulation, the LTE calculation predicts larger temperatures and a smaller plasma volume [18]. Thermal non-equilibrium effects in the discharge are significant in the zone where the Joule heating is maximum (see Figure 8a). On other hand, at the torch exit, the plasma is essentially in thermal equilibrium, though temperatures are significantly lower compared to the corresponding LTE values. This is also evident from the radial profile in the midst of the torch reported in Figure 8b. As for the LTE simulation, the results are in good agreement with the reference solution.

4.3 ICP wind tunnel

After the study of LTE/NLTE plasma torch configurations, a fluid/electromagnetic/material response coupled simulation of an ICP wind tunnel is now considered. The geometry corresponds to that of the Plasmatron facility at the von Karman Institute for Fluid Dynamics (Belgium) [74]. The calculation assumes, again, axi-symmetric flow without swirl. The NLTE plasma model is the same as that of Sec. 4.2 with the inclusion of C, CO and CO_2 to account for pyrolysis within the TPS sample. For the sake of simplicity, ablation and material recession are neglected.

The operating conditions are:

- $p_\infty = 5000\,\mathrm{Pa}$,
- $\dot{m} = 16\,\mathrm{g/s}$,
- $P_t = 150\,\mathrm{kW}$,
- $f = 0.37\,\mathrm{MHz}$,
- $T_w = 350\,\mathrm{K}$,
- TPS material: TACOT [94].

The solution of the coupled problem is computed as follows:

1. Obtain first a steady-state flowfield by coupling only HEGEL and FLUX as done in Sec. 4.2.
2. Restart the previous solution by including PATO. HEGEL is still run using local time-stepping to achieve steady-state, whereas PATO is run in unsteady fashion using a time-step of 0.1 ms. This approximation, to be further investigated in future work, may be justified based on the fact that the plasma dynamics and material response time-scales are very different. The duration of the time window to exchange surface data is set to 10 ms, meaning that surface quantities are communicated every 100 fluid iterations. For volume coupling, data are instead passed every 1000 iterations as the plasma discharge is little affected by the material response.

Figure 9 shows the time-history of the plasma temperature, pressure inside the TPS sample, and mole fraction of CO resulting from pyrolysis.

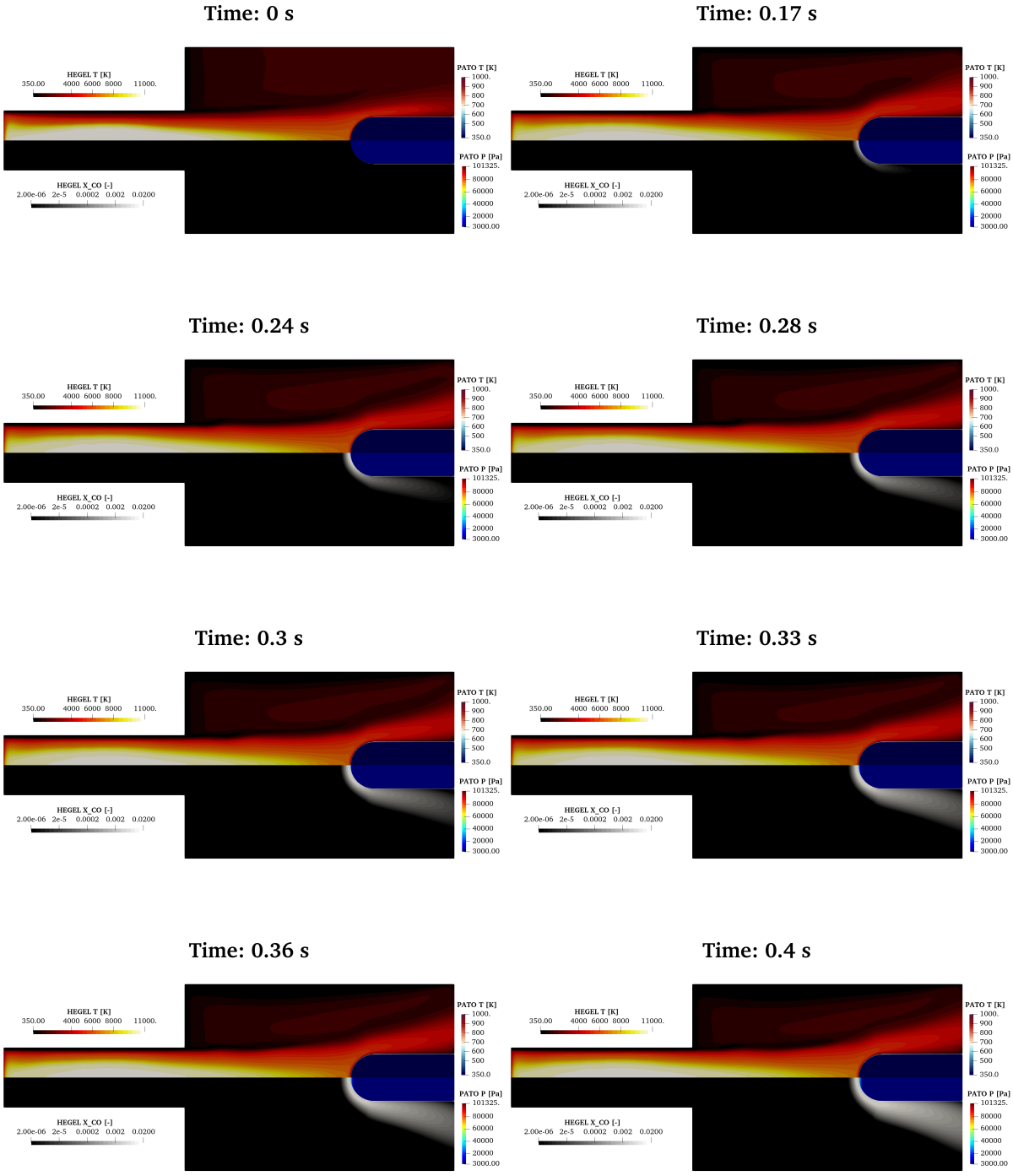

Figure 9: ICP wind tunnel simulation: time history of plasma temperature, pressure inside the TPS sample and mole fraction of CO resulting from pyrolysis.

5 Conclusions and future work

This paper has presented and discussed the development of a multi-physics framework for inductively coupled plasma (ICP) wind tunnels. As opposed to a monolithic approach, three solvers responsible for the evolution of: (i) the plasma, (ii) the electromagnetic field, and (iii)

the thermophysical properties of the material sample, have been coupled using the preCICE library. After assessing the correct implementation via verification benchmarks, the feasibility of the proposed methodology has been demonstrated for two-dimensional axi-symmetric configurations.

Future work will focus on extending the developed framework to three-dimensional and unsteady scenarios, inclusion of ablation and material recession, and model validation via comparison against experiments performed at the CHESS Plasmatron X facility .

Acknowledgments

This work was supported by the Center for Hypersonics and Entry Systems Studies (CHESS) at University of Illinois at Urbana-Champaign.

References

[1] P. Fauchais. Understanding plasma spraying. *J. Phys. D: Appl. Phys.*, 37(9):R86, 2004.

[2] J. Heberlein and A. B. Murphy. Thermal plasma waste treatment. *J. Phys. D: Appl. Phys.*, 41(5):053001, 2008.

[3] A. B. Murphy, M. Tanaka, K. Yamamoto, S. Tashiro, T. Sato, and J. J. Lowke. Modelling of thermal plasmas for arc welding: the role of the shielding gas properties and of metal vapour. *J. Phys. D: Appl. Phys.*, 42(19):194006, 2009.

[4] V. Colombo, A. Concetti, E. Ghedini, S. Dallavalle, and M. Vancini. High-speed imaging in plasma arc cutting: a review and new developments. *Plasma Sources Sci. Technol.*, 18(2):023001, 2009.

[5] M. Shigeta and A. B. Murphy. Thermal plasmas for nanofabrication. *J. Phys. D: App. Phys.*, 44(17):174025, 2011.

[6] T. B. Reed. Induction coupled plasma torch. *J. Appl. Phys.*, 32(5):821–824, 1961.

[7] J. Mostaghimi and M. I. Boulos. In *Inductively Coupled Plasma in Analytical Spectrometry*, pages 949–984, 1992.

[8] M. I. Boulos, P. Fauchais, and E. Pfender. *Thermal plasmas: Fundamentals and Applications. Volume 1.* Spinger, 1994.

[9] M. I. Boulos. Flow and temperature fields in the fire-ball of an inductively coupled plasma. *IEEE Trans. Plasma Sci.*, 4(1):28–39, 1976.

[10] J. Mostaghimi, P. Proulx, and M. I. Boulos. Parametric study of the flow and temperature fields in an inductively coupled r.f. plasma torch. *Plasma Chem. Plasma Process.*, 4(3):199–217, 1984.

[11] J. Mostaghimi and M. I. Boulos. Two-dimensional electromagnetic field effects in induction plasma modeling. *Plasma Chem. Plasma Process.*, 9(1):25–44, 1989.

[12] T. Watanabe, K. Yanase, T. Honda, and A. Kanzawa. The flow, temperature and concentration fields in a radio-frequency Argon-Helium plasma. *J. Chem. Eng. Jpn.*, 23(4):389–395, 1990.

[13] D. Bernardi, V. Colombo, E. Ghedini, and A. Mentrelli. Three-dimensional modelling of inductively coupled plasma torches. *Eur. Phys. J. D*, 22(1):119–125, 2003.

[14] V. Colombo, A. Concetti, E. Ghedini, M. Gherardi, and P. Sanibondi. Three-dimensional time-dependent large eddy simulation of turbulent flows in an inductively coupled thermal plasma torch with a reaction chamber. *IEEE Trans. Plasma Sci. IEEE Nucl. Plasma Sci. Soc.*, 39(11):2894–2895, 2011.

[15] E. Rinaldi, R. Pecnik, and P. Colonna. Exact Jacobians for implicit Navier-Stokes simulations of equilibrium real gas flows. *J. Comput. Phys.*, 270:459–477, 2014.

[16] E. Pfender, J. Fincke, and R. Spores. Entrainment of cold gas into thermal plasma jets. *Plasma Chem. Plasma Process.*, 11(4):529–543, 1991.

[17] W. Zhang, A. Lani, H. B. Chew, and M. Panesi. Modeling of non-equilibrium plasmas in an inductively coupled plasma facility. AIAA Paper 2014–2235, 2014. 45th AIAA Plasmadynamics and Lasers Conference, Atlanta, GA.

[18] W. Zhang, A. Lani, and M. Panesi. Analysis of non-equilibrium phenomena in inductively coupled plasma generators. *Phys. Plasmas*, 23(7):073512, 2016.

[19] A. Munafò, S. A. Alfuhaid, , J.-L. Cambier, and M. Panesi. A tightly coupled non-equilibrium model for inductively coupled radio-frequency plasmas. *J. Appl. Phys.*, 118(13):133303, 2015.

[20] M. Shigeta. Turbulence modeling of thermal plasma flows. *J. Phys. D: Appl. Phys.*, 49(49):493001, 2016.

[21] A. Munafò, A. Alberti, C. Pantano, J. B. Freund, and M. Panesi. A computational model for nano-second pulse laser-plasma interactions. *J. Comput. Phys.*, 406:109190, 2020.

[22] S. Kumar, A. Munafò, N. Mansour, and M. Panesi. Self-consistent magneto-hydrodymamic modeling of ICP discharges. AIAA paper 2022-1619, 2022. AIAA SciTech Forum, San Diego, CA.

[23] J. Lachaud and N. N. Mansour. Porous-material analysis toolbox based on openfoam and applications. *J. Thermophys. Heat Transfer*, 28(2):191–202, 2014.

[24] H.-J. Bungartz, F. Lindner, B. Gatzhammer, M. Mehl, K. Scheufele, A. Shukaev, and B. Uekermann. preCICE – a fully parallel library for multi-physics surface coupling. *Comp. Fluids*, 141:250–258, 2016. Advances in Fluid Structure Interaction.

[25] C. Park. *Nonequilibrium Hypersonic Aerothermodynamics*. Wiley, New York, NY, 1990.

[26] M. Capitelli, C. M. Ferreira, B. F. Gordiets, and A. I. Osipov. *Plasma Kinetics in Atmospheric Gases*. Springer, 2000.

[27] A. Bultel, B. van Ootegem, A. Bourdon, and P. Vervisch. Influence of Ar_2^+ in an argon collisional-radiative model. *Phys. Rev. E*, 65(4):046406, 2002.

[28] M. Capitelli, I. Armenise, D. Bruno, M. Cacciatore, R. Celiberto, G. Colonna, O. De Pascale, P. Diomede, F. Esposito, C. Gorse, K. Hassouni, A. Laricchiuta, S. Longo, D. Pagano, L. D. Pietanza, and M. Rutigliano. Non-equilibrium plasma kinetics: a state-to-state approach. *Plasma Sources Sci. Technol.*, 16(1):30–44, 2007.

[29] J. G. Kim, O. J. Kwon, and C. Park. Master equation study and nonequilibrium chemical reactions for $H + H_2$ and $He + H_2$. *J. Thermophys. Heat Transfer*, 23(3):443–453, 2009.

[30] J. G. Kim, , and O. J. Kwon C. Park. Master equation study and nonequilibrium chemical reactions for $H + H_2$ and $H + He$. *J. Thermophys. Heat Transfer*, 23(3):443–453, 2009.

[31] M. Panesi, T. E. Magin, A. Bourdon, A. Bultel, and O. Chazot. Fire II flight experiment analysis by means of a collisional-radiative model. *J. Thermophys. Heat Transfer*, 23(2):236–248, 2009.

[32] M. Panesi, T. E. Magin, A. Bourdon, A. Bultel, and O. Chazot. Electronic excitation of atoms and molecules for the FIRE II flight experiment. *J. Thermophys. Heat Transfer*, 25(3):361–374, 2011.

[33] L. D. Pietanza, G. Colonna, A. De Giacomo, and M. Capitelli. Kinetic processes for laser induced plasma diagnostic: a collisional-radiative model approach. *Spectrochim. Acta Part B*, 65:616–626, 2010.

[34] A. Munafò, M. Panesi, R. L. Jaffe, G. Colonna, A. Bourdon, and T. E. Magin. QCT-based vibrational collisional models applied to nonequilibrium nozzle flows. *Eur. Phys. Jour. D*, 66:188, 2012.

[35] A. Munafò, A. Lani, A. Bultel, and M. Panesi. Modeling of non-equilibrium phenomena in expanding flows by means of a collisional-radiative model. *Phys. Plasmas*, 20(7):073501, 2013.

[36] M. Panesi, R. L. Jaffe, D. W. Schwenke, and T. E. Magin. Rovibrational internal energy transfer and dissociation of $N(^4S_u) + N_2(^1\Sigma_g^+)$ system in hypersonic flows. *J. Chem. Phys*, 138(4):044312, 2013.

[37] A. Bultel and J. Annaloro. Elaboration of collisional-radiative models for flows related to planetary entries into the Earth and Mars atmospheres. *Plasma Sources Sci. Technol.*, 22(2):025008, 2013.

[38] M. Panesi, A. Munafò, T. E. Magin, and R. L. Jaffe. Study of the non-equilibrium shock heated nitrogen flows using a rovibrational state-to-state method. *Phys. Rev. E*, 90:013009, 2014.

[39] Jason D. Bender, Paolo Valentini, Ioannis Nompelis, Yuliya Paukku, Zoltan Varga, Donald G. Truhlar, Thomas Schwartzentruber, and Graham V. Candler. An improved potential energy surface and multi-temperature quasiclassical trajectory calculations of $N_2 + N_2$ dissociation reactions. *J. Chem. Phys.*, 143(5):054304, 2015.

[40] H. Luo, M. Kulakhmetov, and A. Alexeenko. *Ab initio* state-specific N_2+O dissociation and exchange modeling for molecular simulations. *J. Chem. Phys.*, 146(7):074303, 2017.

[41] S. M. Jo, S. Venturi, M. P. Sharma, A. Munafò, and M. Panesi. Rovibrational-specific QCT and master equation study on $N_2(X^1\Sigma_g^+) + O(P)$ and $NO(X^2\Pi) + N(4^S)$ systems in high-energy collisions. *J. Phys. Chem. A*, 126(21):3273–3290, 2022.

[42] G. Colonna, I. Armenise, D. Bruno, and M. Capitelli. Reduction of state-to-state kinetic to macroscopic models in hypersonic flows. *J. Thermophys. Heat Transfer*, 20(3):477–486, 2006.

[43] A. Munafò, M. Panesi, and T. E. Magin. Boltzmann rovibrational collisional coarse-grained model for internal energy excitation and dissociation in hypersonic flows. *Phys. Rev. E*, 89(2):023001, 2014.

[44] A. Munafò and T. E. Magin. Modeling of stagnation-line nonequilibrium flows by means of quantum based collisional models. *Phys. Fluids*, 26(9):097102, 2014.

[45] Y. Liu, M. Panesi, A. Sahai, and M. Vinokur. General multi-group macroscopic modeling for thermo-chemical non-equilibrium gas mixtures. *J. Chem. Phys.*, 142(13):134109, 2015.

[46] A. Munafò, Y. Liu, and M. Panesi. Physical models for dissociation and energy transfer in shock-heated nitrogen flows. *Phys. Fluids*, 27(12):127101, 2015.

[47] A. Munafò, N. N. Mansour, and M. Panesi. A reduced-order NLTE kinetic model for radiating plasmas of outer envelopes of stellar atmospheres. *Astrophys. J.*, 838(2):126, 2017.

[48] A. Sahai, B. Lopez, C. O. Johnston, and M. Panesi. Adaptive coarse graining method for energy transfer and dissociation kinetics of polyatomic species. *J. Chem. Phys.*, 147(5):054107, 2017.

[49] R. L. Macdonald, R. L. Jaffe, D. W. Schwenke, and M. Panesi. Construction of a coarse-grain quasi-classical trajectory method. I. Theory and application to N_2-N_2 system. *J. Chem. Phys.*, 148(5):054309, 2018.

[50] R. L. Macdonald, M. S. Grover, T. E. Schwartzentruber, and M. Panesi. Construction of a coarse-grain quasi-classical trajectory method. II. Comparison against the direct molecular simulation method. *J. Chem. Phys.*, 148(5):054310, 2018.

[51] A. Sahai, C. O. Johnston, B. Lopez, and M. Panesi. Flow-radiation coupling in CO_2 hypersonic wakes using reduced-order non-Boltzmann models. *Phys. Rev. Fluids*, 4(9):093401, 2019.

[52] M. P. Sharma, Y. Liu, and M. Panesi. Coarse-grained modeling of thermochemical nonequilibrium using the multigroupmaximum entropy quadratic formulation. *Phys. Rev. E*, 101(1):013307, 2020.

[53] S. Venturi, M. P. Sharma, B. Lopez, and M. Panesi. Data-inspired and physics-driven model reduction for dissociation: Application to the $O_2 + O$ system. *J. Phys. Chem. A*, 124(41):8359–8372, 2020.

[54] S. Venturi, R. L. Jaffe, and M. Panesi. Bayesian machine learning approach to the quantification of uncertainties on ab initio potential energy surfaces. *J. Phys. Chem. A*, 124(25):5129–5146, 2020.

[55] J. G. Kim and S. M. Jo. Modification of chemical-kinetic parameters for 11-air species in re-entry flows. *Int. J. Heat Mass Transf.*, 169:120950, 2021.

[56] I. Zanardi, S. Venturi, and M. Panesi. Towards efficient simulations of non-equilibrium chemistry in hypersonic flows: a physics-informed neural network framework. AIAA paper 2022-1639, 2022. AIAA SciTech Forum, San Diego, CA.

[57] J. H. Ferziger and H. G. Kaper. *Mathematical Theory of Transport Processes in Gases.* North-Holland Pub. Co., 1972.

[58] V. Giovangigli. *Multicomponent Flow Modeling*. Birkhäuser, Berlin, 1999.

[59] E. Nagnibeda and E. Kustova. *Non-Equilibrium Reacting Gas Flows*. Springer, Berlin, 2009.

[60] R. S. Devoto. Transport properties of ionized monatomic gases. *Phys. Fluids*, 9(6):1230–1240, 1966.

[61] R. S. Devoto. Transport coefficients of partially ionized Argon. *Phys. Fluids*, 10(2):354–364, 1967.

[62] T. E. Magin and G. Degrez. Transport algorithms for partially ionized and unmagnetized plasmas. *J. Comput. Phys.*, 198(2):424–449, 2004.

[63] T. E. Magin and G. Degrez. Transport properties of partially ionized and unmagnetized plasmas. *Phys. Rev. E*, 70(4):046412, 2004.

[64] D. Bruno, C. Catalfamo, O. De Pascale M. Capitelli and, G. Colonna and, P. Diomede, C. Gorse, A. Laricchiuta, S. Longo, D. Giordano, and F. Pirani. Transport properties of high-temperature Jupiter atmosphere components. *Phys. Plasmas*, 17(11):112315, 2010.

[65] M. Capitelli, D. Bruno, and A. Laricchiuta. *Fundamantal Aspects of Plasma Physics: Transport*, volume 74 of *Springer Series on Atomic, Optical, and Plasma Physics*. Springer, Heidelberg, 2013.

[66] Y. B. Zel'dovich and Yu. P. Raizer. *Physics of Shock Waves and High-Temperature Hydrodynamic Phenomena*. Academic Press Inc., New York, NY, 1967.

[67] Y. Liu and M. Vinokur. Nonequilibrium flow computations. I. An analysis of numerical formulations of conservation laws. *J. Comput. Phys.*, 83(2):373–397, 1989.

[68] B. Grossman and P. Cinnella. Flux-split algorithms for flows with non-equilibrium chemistry and vibrational relaxation. *J. Comput. Phys.*, 88(1):131–168, 1990.

[69] H. B. Callen. *Thermodynamics and an Introduction to Thermostatistics*. John Wiley & Sons, New York, NY, 1985. Second edition.

[70] C. Park. Review of chemical-kinetic problems of future NASA missions, I: Earth entries. *J. Thermophys. Heat Transfer*, 7(3):385–398, 1993.

[71] W. J. Vincenti and C. H. Kruger. *Introduction to Physical Gasdynamics*. Wiley, New York, NY, 1965.

[72] J. D. Anderson. *Hypersonic and High Temperature Gasdynamics*. McGraw-Hill, New York, NY, 1989.

[73] P. A. Gnoffo, R. N. Gupta, and J. L. Shinn. Conservation equations and physical models for hypersonic air flows in thermal and chemical nonequilibrium. NASA Technical Paper 2867, 1989.

[74] D. Vanden Abeele. *An Efficient Computational Model for Inductively Coupled Air Plasma Flows Under Thermal and Chemical Non-Equilibrium*. PhD thesis, Univesité Libre de Bruxelles, Bruxelles, Belgium, 2000.

[75] D. Vanden Abeele and G. Degrez. Efficient computational model for inductive plasma flows. *AIAA Journal*, 38(2):234–242, 2000.

[76] A. Alberti, A. Munafò, M. Koll, M. Nishihara, C. Pantano, J. B. Freund, G. S. Elliott, and M. Panesi. Laser-induced non-equilibrium plasma kernel dynamics. *J. Phys. D: Appl. Phys.*, 53(2):025201, oct 2019.

[77] S. Balay, S. Abhyankar, M. F. Adams, J. Brown, P. Brune, K. Buschelman, L. Dalcin, A. Dener, V. Eijkhout, W. D. Gropp, D. Karpeyev, D. Kaushik, M. G. K., D. A. May, L. C. McInnes, R. Tran Mills, T. Munson, K. Rupp, P. Sanan, B. F. Smith, S. Zampini, H. Zhang, and H. Zhang. PETSc Web page. `https://www.mcs.anl.gov/petsc`, 2021.

[78] S. Balay, S. Abhyankar, M. F. Adams, J. Brown, P. Brune, K. Buschelman, L. Dalcin, A. Dener, V. Eijkhout, W. D. Gropp, D. Karpeyev, D. Kaushik, M. G. K., D. A. May, L. C. McInnes, R. Tran Mills, T. Munson, K. Rupp, P. Sanan, B. F. Smith, S. Zampini, H. Zhang, and H. Zhang. PETSc users manual. Technical Report ANL-95/11 - Revision 3.15, Argonne National Laboratory, 2021.

[79] S. Balay, W. D. Gropp, L. C. McInnes, and B. F. Smith. Efficient management of parallelism in object oriented numerical software libraries. In E. Arge, A. M. Bruaset, and H. P. Langtangen, editors, *Modern Software Tools in Scientific Computing*, pages 163–202. Birkhäuser Press, 1997.

[80] C. Hirsch. *Numerical Computation of Internal and External Flows, Volume 1: Fundamentals of Numerical Discretization.* John Wiley & Sons, 1988. First edition.

[81] P. L. Roe. Approximate Riemann solvers, parameter vectors and difference schemes. *J. Comput. Phys.*, 43(2):357–372, 1981.

[82] M. S. Liou. A sequel to AUSM: AUSM$^+$. *J. Comput. Phys.*, 129:364–382, 1996.

[83] C. Hirsch. *Numerical Computation of Internal and External Flows, Volume 2: Computational Methods for Inviscid and Viscous Flows.* John Wiley & Sons, 1990. First edition.

[84] B. van Leer. Towards the ultimate conservative difference scheme. V. A second-order sequel to Godunov's method. *J. Comput. Phys.*, 32(1):101–136, 1979.

[85] G.-S. Jiang and C.-W. Shu. Efficient implementation of weighted ENO schemes. *J. Comput. Phys.*, 126(1):202–228, 1996.

[86] R. Anderson, J. Andrej, A. Barker, J. Bramwell, J.-S. Camier, J. Cerveny V. Dobrev, Y. Dudouit, A. Fisher, Tz. Kolev, W. Pazner, M. Stowell, V. Tomov, I. Akkerman, J. Dahm, D. Medina, and S. Zampini. MFEM: A Modular Finite Element Library. *Comput. Math. with Appl.*, 81:42–74, 2021.

[87] MFEM: Modular finite element methods [Software]. `https://mfem.org`, 2021.

[88] R. N. Rieben and D. A. White. Verification of high-order mixed finite-element solution of transient magnetic diffusion problems. *IEEE Trans. Magn.*, 42(1):25–39, 2005.

[89] *hypre*: High Performance Preconditioners. `https://llnl.gov/casc/hypre`, `https://github.com/hypre-space/hypre`.

[90] OpenFOAM Web page. `https://www.openfoam.com`, 2021.

[91] R. A. Thompson and P. A. Gnoffo. Implementation of a blowing boundary condition in the LAURA code. AIAA Paper 2008–1243, 2008. 46th AIAA Aerospace Sciences Meeting and Exhibit, Reno, NV.

[92] A. Martin and I. D. Boyd. Strongly coupled computation of material response and nonequilibrium flow for hypersonic ablation. *J. Spacecr. Rockets*, 52(1):89–104, 2015.

[93] J. Blazek. *Computational Fluid Dynamics: Principles and Applications*. Butterworth-Heinemann, 2015. Third edition.

[94] R. Chiodi, K. Stephani, M. Panesi, and D. J. Bodony. CHyPS: A high-order material response solver for ablative thermal protection systems. AIAA paper 2022-1501, 2022. AIAA SciTech Forum, San Diego, CA.

A Analytical solution for the conjugate heat transfer problem

The temperature solution for the conjugate heat transfer problem of Sec. 4.1 is given the sum of the steady profile and a time-dependent term:

$$T(x,\,t) = \tilde{T}(x) + T^{\star}(x,\,t), \tag{33}$$

where:

$$\tilde{T}(x) = T_l + (T_r - T_l)\frac{x}{L}, \tag{34}$$

$$T^{\star}(x,\,t) = \frac{2}{\pi}(T_r - T_l)\sum_{n=1}^{+\infty}(-1)^n \sin\left(\frac{2n\pi x}{L}\right)\exp\left[-\left(\frac{2n\pi}{L}\right)^2 \alpha t\right], \tag{35}$$

with the medium thermal diffusivity being $\alpha = \lambda/\rho\,C$.